Geophys. J. R. astr. Soc. (1987) **90**, 445–465

Mechanisms of isostatic compensation in the vicinity of the East African Rift, Kenya

Timothy D. Bechtel and Donald W. Forsyth *Department of Geological Sciences, Brown University, Providence, RI 02912, USA*

Christopher J. Swain *Department of Physics, University of Zimbabwe, Harare, Zimbabwe*

Accepted 1987 January 14. Received 1987 January 14; in original form 1986 June 26

Summary. The topography and gravity anomalies in the area surrounding the East African Rift in Kenya can be modelled as the sum of the effects of surface and subsurface loading of an elastic plate. Assuming surface and subsurface loading are independent processes, the observed coherence between the 2-D Fourier transforms of Bouguer gravity and topography provides a constraint on the effective elastic thickness or flexural rigidity of the plate. Distinct linear segments of the log gravity power spectrum suggest that components of the gravity field with wavelengths of 250–1000 km are generated predominantly by a density contrast at a depth of about 32 km. Most shorter wavelength gravity anomalies are probably associated with source depths of less than 1 km and indicate variations in thickness of low density sedimentary or volcanic layers or lateral variations in density of the surface rocks. A simple density model based on these estimates and the geology of Kenya consists of a cover layer averaging 0.5 km thick with density 2300 kg m^{-3}, a layer 32 km thick with density 2800 kg m^{-3}, and an underlying half-space with density 3200 kg m^{-3}. Using this density model and assuming loading due to relief on all three density interfaces, the elastic thickness that best predicts the observed coherence in the least squares sense is 25 km (Flexural rigidity of 1.4×10^{23} Nm). Amplitudes of loads on the density interfaces can be calculated based on the model response. Topography with wavelength greater than 650 km is locally compensated making surface and subsurface loading indistinguishable. At shorter wavelengths, rift volcanics and volcanic cones including Mts Kenya, Elgon and Kilimanjaro can be identified as surface loads. The largest amplitude subsurface load is an upward directed, regionally supported load beneath the Kenya Dome that may correspond to a region of hot, low density mantle recognized by other geophysical studies. In creating the topography for which surface and sub-

surface loading are distinguishable, surface loading is much more important than doming due to subsurface loading.

Key words: Kenya, gravity, coherence, flexural rigidity, subsurface loading

Introduction

The East African Rift has two main segments (Fig. 1). The eastern branch extends from the Afar triple junction through Ethiopia and western Kenya into Tanzania. The western branch circles to the west of Lake Victoria through Uganda and Tanzania where it merges with the eastern branch in a broad zone of widely spaced faults. Lake Victoria lies on the East African Plateau which is an elevated region fringed by the eastern and western branches of the rift. In Kenya, the Kenya Dome is superimposed on the slope at the edge of the plateau and represents a region where the flanks of the rift are uplifted. The dome is centred roughly on the intersection of the N–S trending Gregory Rift with the ENE–WSW Kavirondo Rift in south-western Kenya (Fig. 1). It has commonly been claimed that the Kenya Dome is the result of episodic domal uplift caused by thermal anomalies in the mantle beneath the rift (e.g. Baker & Wohlenberg 1971). Sedimentary patterns and apparent warping of end-Cretaceous to Quarternary erosion surfaces have been cited as evidence that major uplift of the dome occurred near the Tertiary/Quaternary boundary with intermittent flexing on a smaller scale continuing into the lower Pleistocene (Saggerson & Baker 1971; McCall, Baker & Walsh 1967; Issac 1967). However, there is a voluminous and complex history of shield

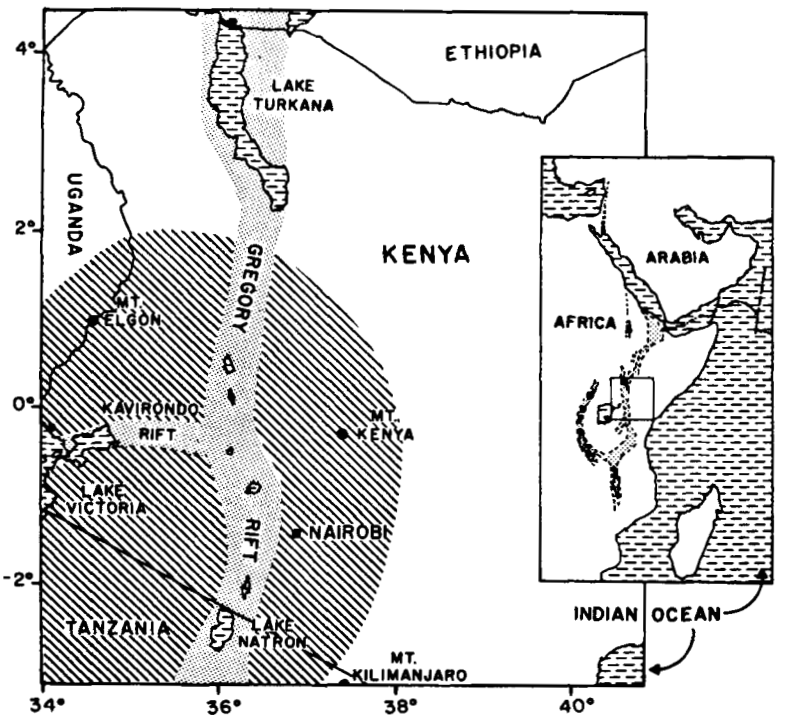

Figure 1. Geography of the study area. Inset (after Baker *et al.* 1972) shows the positions of the Gregory and Kavirondo Rifts in relation to the East African Rift system. Rift areas are stippled on both the map and inset. Diagonal ruling gives the approximate extent of the Kenya Dome.

and rift volcanism associated with the rift and the dome (see Baker, Mohr & Williams 1972) and recent studies of basement contours (King 1978; Williams 1978) suggest that the major portion of the relief of the Kenya Dome results not from uplift but from accumulation of volcanics.

The isostatic compensation of the Kenya dome was first demonstrated by Bullard (1936) using gravity data. Forward modelling of the regional gravity low in Kenya has suggested the presence of anomalous mantle beneath the dome (Fairhead 1976; Darracott, Fairhead & Girdler 1972; Searle 1970). The possibility of anomalous mantle as at least partial compensation for the Kenya Dome has been supported by other geophysical observations. Anomalously slow *P* and *S* velocities are observed at depths greater than 20–40 km beneath the rift (Savage & Long 1985; Nolet & Mueller 1982; Long & Backhouse 1976; Knopoff & Schlue 1972 among others). In particular, Maguire & Long (1976) have mapped the shape of of an anomalous mantle zone that underlies the Kenya Dome. Magnetotellurics and geomagnetic deep soundings indicate that beneath the rift and the dome there exist anomalously high mantle-conductivities (Banks & Beamish 1979; Rooney & Hutton 1977; Beamish 1977; Banks & Ottey 1974). There is also very high heat-flow and hydrothermal activity in the vicinity of the rift (Baticci & Morgan 1986; Skinner 1977), with the bulk of the hydrothermal heat flow centred on the Kenya Dome (Crane & O'Connell 1983). In addition, the mantle densities required by the gravity modelling and the observed mantle *P* velocities do not follow the Nafe–Drake relationship. They can be reconciled by assuming that the anomalous mantle is partially molten (Fairhead 1976). These observations all indicate the presence of hot, partially molten, low density mantle beneath the dome. It has often been suggested that the anomalous mantle is an asthenospheric plume or diapir that has penetrated the lithosphere possibly to the base of the crust.

Having established the presence of anomalous mantle as at least partial compensation for the dome, there are two main problems to address. The first is to determine the relative importance of surface loading (e.g. volcanic construction) versus subsurface loading (e.g. domal uplift) in the creation of the topography of the dome, and the second is to develop a mechanical model of how density anomalies support the topography.

Banks & Swain (1978) and Swain (1979) developed a local compensation model that attempted to match the observed admittance between gravity and topography in Kenya. The admittance or linear transfer function is simply the Fourier transform of the linear filter operating on the topography that best predicts the gravity field in the least-squares sense and is thus a convenient way to describe the relationship between topography and the gravity anomalies that are associated with the isostatic compensation of the topography (Banks, Parker & Huestis 1977; McKenzie & Bowin 1976; Dorman & Lewis 1970). Assuming local compensation, Banks & Swain (1978) concluded that compensation begins no deeper than 55 km and that 50 per cent of the compensation is no deeper than 100 km. If the density contrast responsible for the compensation lies entirely within the mantle and is due to partial melting, a melt fraction of about 6 per cent is suggested (Banks & Swain 1978).

Forsyth (1985) demonstrated that interpretation of the admittance function may yield a biased model of the compensation mechanism if there is both surface and subsurface loading of the lithosphere. Considering both the admittance and the coherence between topography and gravity, the preferred isostatic model is the flexure of an elastic plate overlying an inviscid substrate under applied surface and subsurface loads. The best-fitting flexural model of the admittance and coherence data from Kenya consists of a plate with an effective elastic thickness of 25–30 km and with surface and subsurface loading roughly equal in importance (Forsyth 1985).

The purpose of this study is to re-examine the mechanisms of isostatic compensation in

the vicinity of the East African Rift using the original, complete gravity and topography data of Banks & Swain (1978) and Swain (1979). Using only the admittance and coherence data it was necessary to assume a uniform ratio between the amplitudes of surface and subsurface loading in the formulation of Forsyth (1985). With the complete gravity and topography fields, it is possible not only to estimate the flexural rigidity of the lithosphere, but also to derive maps of the distribution of surface and subsurface loads. Thus, we also address the question of the origin and compensation of individual topographic features.

Isostatic model

The admittance method of studying isostasy was developed by Dorman & Lewis (1970) and McKenzie & Bowin (1976) and involves calculation of the linear transfer function between the harmonic components of topography and gravity. The observed admittance is then compared with that predicted by models of regional isostasy assuming different lithospheric flexural rigidities (local isostasy occurring for zero flexural rigidity). Occasionally the effective elastic thickness T is used instead of the flexural rigidity D. These are equivalent since the flexural rigidity of a thin elastic plate is given by

$$D = ET^3/[12(1-\nu^2)], \tag{1}$$

where E is Young's modulus and ν is Poisson's ratio. Using this approach, admittance studies of various continental regions have yielded estimates of the rigidity of continents of $D = 10^{19}$–10^{22} Nm (McNutt 1980; McNutt & Parker 1978; Banks *et al.* 1977). This is much weaker than the estimates of $D = 10^{23}$–10^{24} Nm obtained by studying individual flexural features on continents (Nakiboglu & Lambeck 1983; Karner & Watts 1983; Passey 1981; Haxby, Turcotte & Bird 1978; Walcott 1970).

There are three primary reasons for this discrepancy. First, the observed admittance is averaged over profiles or wavebands to minimize biasing by noise in the data. When the average includes several provinces with differing flexural rigidity, the provinces are weighted in the average by the square of the amplitude of the topography, discounting the contribution of potentially rigid areas with little topography such as continental shields (Forsyth 1981). Secondly, admittance models have usually assumed surface topographic loading of an elastic plate, whereas subsurface mass anomalies also act as loads and can have a large effect on the admittance (Forsyth 1985; McNutt 1983; Louden & Forsyth 1982). If both mechanisms of loading are important, there is a systematic bias towards low estimates of the flexural rigidity (Forsyth 1985). Finally, the coherence between gravity and topography at short wavelengths is very low. Thus even if an isostatic model with a single form of loading can predict the admittance perfectly, there is a substantial fraction of the gravity field that cannot be accounted for by the model.

Forsyth (1985) has described a method for studying isostasy based on the interpretation of the observed coherence between gravity and topography. Analysing the coherence rather than the admittance avoids the previous problems with weighting and biasing. In addition, by considering both surface and subsurface loading the entire gravity signal can be accounted for, leaving no isostatic anomalies. We have used Forsyth's method to study isostasy in an approximately 880 km^2 area including all of Kenya. The method is especially desirable since previous studies have suggested that surface loading of the lithosphere by volcanic construction and subsurface loading due to the presence of anomalous mantle may be very important in the region of the rift and the Kenya Dome. Using a simple extension of Forsyth's derivation to consider loading on two density contrasts at depth, we have performed an inversion for the best fitting elastic response for the Kenyan lithosphere and

the distribution of surface and subsurface loads. Mathematical notation will follow Forsyth (1985), which is the source for more detailed justification and derivation of the model.

Data

The Bouguer gravity data including terrain corrections were compiled by the Universities of Leicester and Newcastle (Swain & Khan 1978) and gridded by Banks & Swain (1978) with improvements by Swain (1979). There are at least 50 actual measurements in nearly all 1° squares in Kenya. The topography was digitized from 1:50000 maps except in areas of little relief where actual gravity station heights were used. The topography data was smoothed to minimize aliasing (Swain 1979). The final interpolated grids (Figs 2 and 3) were 41 × 46 points with spacing roughly 18 km.

The gridded data was transformed using a 2-D FFT to obtain the amplitudes of Bouguer gravity and topography. It was found that the least spectral leakage was obtained by mirroring the gridded data both N–S and E–W before transforming. This was preferred over tapering or ramping because these cause loss of data on the edges of grids.

The observed coherence was calculated from the powers of topography and gravity

$$E_0(\bar{k}) = \langle H(k)H(k)^* \rangle \tag{2}$$

$$E_1(\bar{k}) = \langle G(k)G(k)^* \rangle \tag{3}$$

and the cross spectrum

$$C(\bar{k}) = \langle G(k)H(k)^* \rangle, \tag{4}$$

where H and G are the Fourier amplitudes of topography and gravity, k (= 2π/wavelength) is the 2-D wavenumber [$=(k_x^2 + k_y^2)^{1/2}$], the * indicates complex conjugation, angle brackets

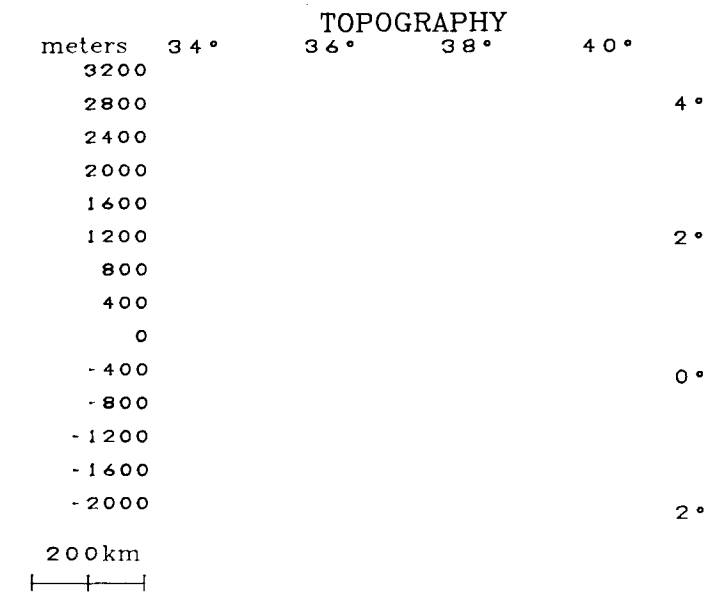

Figure 2. Topography of the study area (from Swain 1979; Banks & Swain 1978). Dark lines are the major faults that bound the rift. Note the generally high topography of the Kenya Dome bisected by the rift valley, and the volcanic cones of Mts Kenya, Elgon and Kilimanjaro. Arrows mark the end points of the cross sections of Fig. 15.

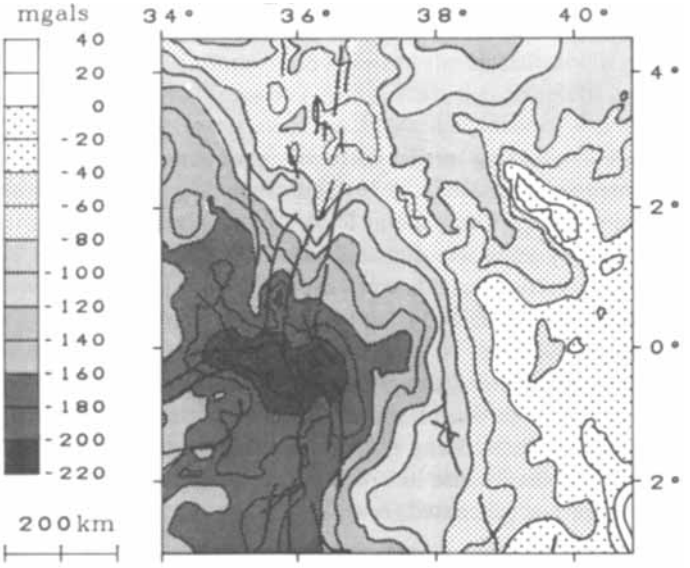

Figure 3. Bouguer gravity map of the study area (from Swain 1979; Banks & Swain 1978). Dark lines are the major rift bounding faults. Note the regional gravity low over the Kenya Dome.

denote averaging over wavebands and $\bar{k}$ is the average k for a waveband. The coherence is then defined as

$$\gamma_0^2(\bar{k}) = C^2(\bar{k})/[E_0(\bar{k})E_1(\bar{k})] \tag{5}$$

(McKenzie & Bowin 1976). Since this estimate tends to be positively biased by noise (Munk & Cartwright 1966), an unbiased estimate was obtained from

$$\gamma^2 = (n\gamma_0^2 - 1)/(n - 1), \tag{6}$$

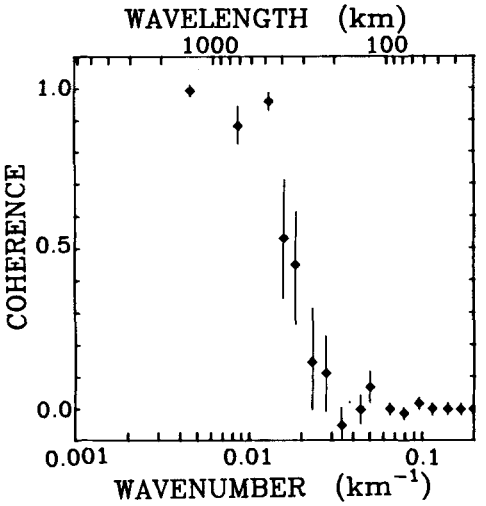

Figure 4. Observed coherence between Bouguer gravity and topography for Kenya as a function of wavenumber. Bars represent one standard error for each coherence average. For wavenumber k, the wavelength is given by $2\pi/k$.

where n is the number of independent Fourier coefficients in the waveband. The standard errors of the coherence estimates were calculated as

$$\Delta\gamma^2 = (1 - \gamma_0^2)(2\gamma_0^2/n)^{1/2} \quad (7)$$

(Bendat & Piersol 1980, p. 274).

The unbiased coherence for Kenya averaged between logarithmically spaced waveband boundaries is shown in Fig. 4. The coherence pattern is consistent with a regional compensation model for a given flexural rigidity of the lithosphere. At very long wavelengths, loads create compensating roots making the Bouguer gravity and topography signals coherent. At short wavelengths, loads are supported by the rigidity of the lithosphere and if surface and subsurface loading are statistically independent the coherence goes to zero. At intermediate wavelengths, the position of the transition between coherent and incoherent fields is governed by the characteristic wavelength for flexure of the lithosphere. Fig. 5 reproduces a plot from Forsyth (1985) showing how the position of the fall-off in coherence should shift with changes in the strength of the lithosphere. Thus by matching the observed coherence using a flexural model with surface and subsurface loading of an elastic plate it was possible to invert for the flexural rigidity of the lithosphere in Kenya.

Density model

The model for the gross density structure beneath Kenya used in the inversion for the elastic response was developed from consideration of geology, published geophysical studies and the gravity power spectrum. The geologic map of Kenya (Fig. 6) suggests a simple model of Tertiary and Quaternary extrusive volcanics and sediments overlying relatively more dense high-grade Precambrian basement. The volcanic and sedimentary cover is close to 1 km thick over much of Kenya and may be over 3 km thick in the rift itself (Keller, Khan & Prodehl 1986; King 1978; Williams 1978; Baker *et al.* 1972). The densities used for the cover and basement are rough averages of values obtained from hand specimens, Nafe–Drake estimates

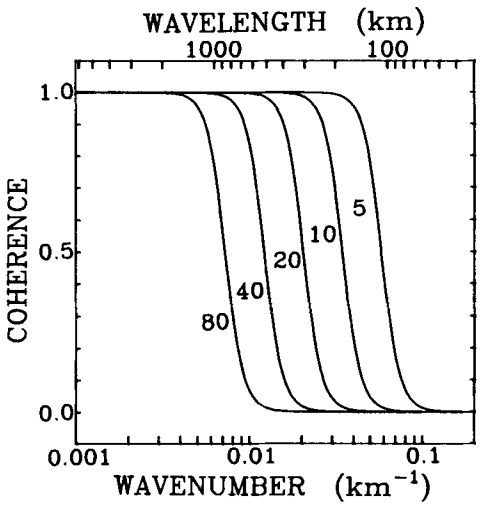

Figure 5. Predicted coherence as a function of wavenumber. Assumes equal amplitudes of surface and subsurface loading and a density contrast of 680 kg m^{-3} at a depth of 35 km. Numbers indicate the effective elastic thickness. The position of the transition from coherent to incoherent gravity and topography is strongly a function of the rigidity of the plate (after Forsyth 1985).

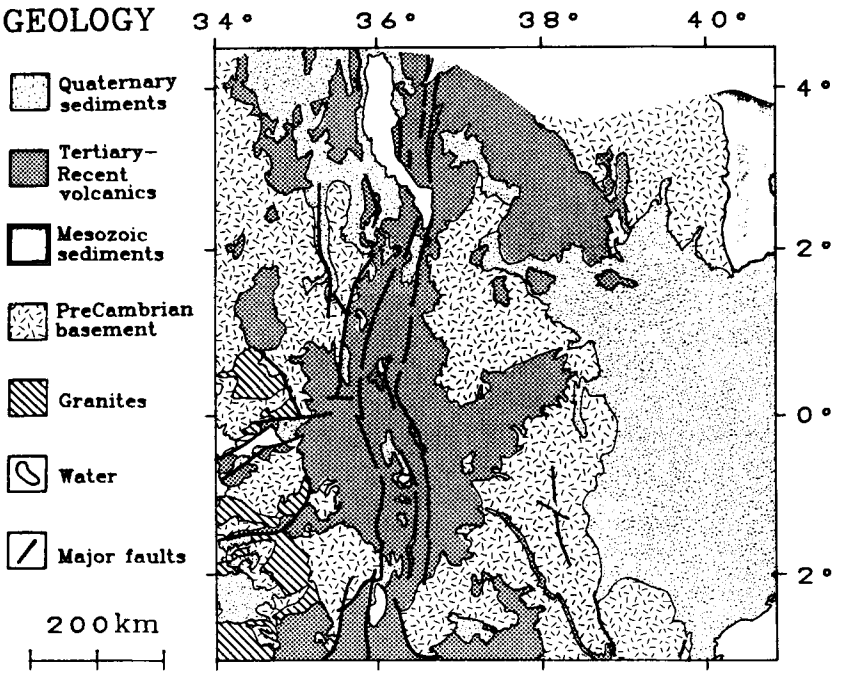

Figure 6. Simplified geology of Kenya compiled from maps published by the Survey of Kenya, Nairobi, Kenya, and the Directorate of Overseas Surveys, London, England. General stratigraphy has Precambrian gneisses, metamorphosed sediments and volcanics unconformably overlain by Tertiary to Recent extrusive volcanics and alluvium.

from seismic studies and mean near-surface density estimates from gravity studies. The range of probable volcanic and sedimentary cover densities is 2000–2500 kg m^{-3} (Swain *et al.* 1981; Swain 1979). Meta-volcanic basement densities may be in the range 2700–2900 kg m^{-3} (Swain 1979; Fairhead 1976; Darracott *et al.* 1972). We chose 2300 and 2800 kg m^{-3} for the densities of cover and basement, respectively. The preferred mantle density of 3200 kg m^{-3} was chosen to be on the low side of normal sub-Moho density estimates of 3200–3400 kg m^{-3} (Ringwood 1975; Woollard 1970). A density of 2670 kg m^{-3} was assumed in calculating the Bouguer anomaly. If this were the wrong average density of the topography, we would expect significant coherence between gravity and topography at short wavelengths and a corresponding non-zero admittance. Both coherence and admittance approach zero at short wavelengths (Fig. 4 and Banks & Swain 1978). Deviations of the average density of the local topography from the assumed mean density for the entire region will appear in our analysis as shallow, subsurface loads.

The average thicknesses of the cover and basement were obtained from the gravity power spectrum. The log gravity power spectrum displays distinct segments (solid lines in Fig. 7). For $k > 0.025$ km^{-1} the power is roughly linear with shallow slope. A second segment covers the range $0.007 < k < 0.025$ km^{-1} and has a steeper slope. A possible third segment at $k < 0.007$ is suggested by about five wavenumbers. Karner & Watts (1983) suggest that linear segments of a gravity power spectrum are due to the power in different wavebands being dominated by signal from different depths. The formula for upward continuation of harmonic relief at a density contrast at depth Z to obtain the gravity signal is

$$G(k) = U(k)2\pi\Delta\rho\Gamma \exp(-kZ), \quad (8)$$

where U is the amplitude of the relief, $\Delta\rho$ is the density contrast and Γ is the gravitational constant. Squaring this and taking the logarithm gives the log gravity power

$$\log G^2(k) = -2Zk + \log U^2(k) + \log (2\pi\Delta\rho\Gamma)^2. \tag{9}$$

Karner & Watts approximate this as a straight line with slope $-2Z$. This assumes that the last two terms on the rhs of (9) are constant, and that the slope of the log gravity power is due solely to the attenuation of high-frequency signal in the relief by upward continuation. In other words, the spectrum of the relief on the density contrast is assumed to be white. However, it is commonly observed that for real surfaces on many scales

$$\log U^2(k) = \mu \log k, \tag{10}$$

where μ is almost always close to -2 (e.g. Sayles & Thomas 1978). Therefore the second term on the rhs of (9) is a function of k, and the slope of a linear segment of the gravity power is the sum of the slope due to upward continuation of the relief at depth and the slope of the power of the relief at depth. To obtain an accurate depth from the gravity power spectrum, it is necessary to remove the effect of the power of U. We have done this by substituting (10) into (9) and considering the normalized log gravity power

$$\log G_n^2(k) = \log G^2(k) - \mu \log k = -2Zk + \text{constants}, \tag{11}$$

where we calculated a value for μ by fitting a least squares line to log topography power versus log wavenumber and obtained a value of $\mu = -2.7$. The depth Z is then given by the slope of a least squares line fit to the lhs of (11). Although subsurface relief or inhomogeneities may not have exactly the same spectrum as the surface topography, we expect that the slope of the log power of relief should not be very different from -2 for any real surface. In any case, our estimate should be better than the assumption of a white spectrum used by Karner & Watts (1983).

Least-squares lines were fit to normalized gravity in the two shorter wavelength wave-

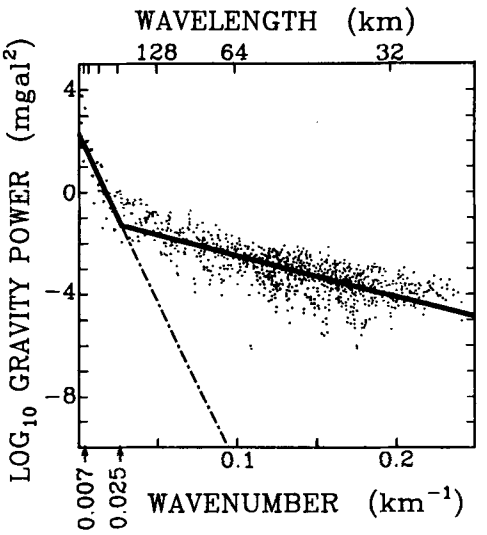

Figure 7. Power spectrum of Bouguer gravity showing two distinct linear segments representing two dominant average source depths for the gravity signal. Solid lines are least squares fits to the two wavebands. Dashed line is the extrapolation of the power in the long wavelength band that is subtracted from the short wavelength band when the signal is split.

bands of Fig. 7 to estimate the average depths to the density contrasts dominating the signal in each waveband. The average depths to density contrasts obtained from (11) are

0.5 km for $0.025 < k$ km^{-1}

32 km for $0.007 < k < 0.025$ km^{-1}.

Although the power at the very longest wavelengths is strongly affected by mirroring, the fact that some points lie above the line for the $0.007 < k < 0.25$ km^{-1} waveband suggests that there may be some contribution to the power at these wavenumbers from a source at a depth of 100 km. The upwarp of the lithosphere–asthenosphere boundary beneath the rift suggested by Dahlheim & Davis (1986) and Halderman, Davis & Dahlheim (1986) on the basis of P and S delays and Q anomalies could contribute the long wavelength power to the gravity spectrum.

The shallow interface does not necessarily have to correspond to the contact between volcanics/sediment and basement, but it is appealing and convenient to refer to it as such. The average depth of 0.5 km obtained from the short wavelength power spectrum is consistent with cover thicknesses ranging from 0 to 2 km over the study region. We used the 32 km depth from the intermediate waveband to fix the average depth to the next deepest density contrast. The value of 32 km is between the range of estimated depths to the seismic Moho of 35–40 km near Nairobi, in northern Tanzania and from the latest KRISP results (Keller *et al.* 1985; Rykounov *et al.* 1972; Bonjer, Fuchs & Wohlenberg 1970) and the 20 km estimate from the rift floor (Griffiths *et al.* 1971). The applied loads at an average depth of 32 km could be lateral variations in temperature, composition or degree of partial melting rather than the relief on the Moho that we have assumed for pictorial and mathematical convenience.

The resulting model of the density structure beneath Kenya used in the inversion for D is depicted in Fig. 8. The relief on the surface density contrast is simply the topography H. Relief on the shallow interface V and at the Moho W were obtained by downward continuation of the Bouguer gravity.

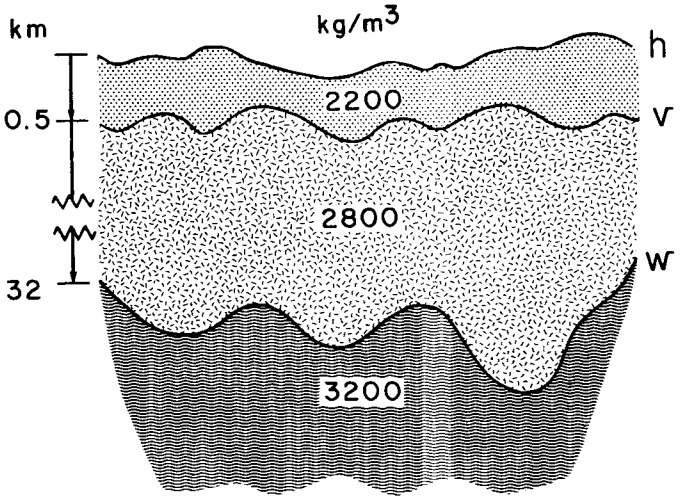

Figure 8. Schematic representation of the density model of the Kenyan crust. The surface relief h is simply the topography. The relief on the two subsurface density contrasts v and w is obtained by downward continuation of the two distinct wavebands of Bouguer gravity (see Fig. 7) to the appropriate depths.

Downward continuation of gravity

Based on the assumption that the power in the gravity spectrum has its source at a shallow density contrast at short wavelengths and at the Moho at longer wavelengths, we obtained the relief on the two interfaces by downward continuation of the two wavebands to 0.5 and 32 km, respectively. The downward continuation formula is given by

$$U(k) = G(k) \exp(kZ)/(2\pi\Delta\rho\Gamma). \tag{12}$$

The exponential dependence on wavenumber and depth often makes downward continuation unstable in the presence of noise at short wavelengths. This was not a problem for our model since short-wavelength data was only continued to 0.5 km depth. Application of (12) to gravity amplitudes in the waveband $0.025 < k$ yielded the relief $V(k)$ on the shallow interface. The waveband $0.007 < k < 0.025$ and (10) produced the Moho relief $W(k)$.

It is important to remember that although there is relief on three density contrasts in this model, there are only two pieces of information. H is observed, but V and W are obtained by splitting the single observable G into two wavebands. The separation of the gravity spectrum into two components was accomplished by extending the linear long wavelength component to shorter wavelengths (dashed line in Fig. 7) and subtracting this theoretical model from the total spectrum at wavenumbers above the 0.025 km^{-1} cut-off. This tapering of the cut-off seems more physically reasonable, and prevents the ringing on the edges of the gridded Moho relief that would occur if an abrupt cut-off truncated the shorter wavelengths of the Moho component of gravity.

Formulation of the isostatic model

Given a model for the density structure beneath Kenya (Fig. 8) and assuming that the lithosphere behaves as an elastic plate with some flexural rigidity D, we can predict the coherence between gravity and topography. In practice, the coherence was predicted as part of a least-squares inversion for D.

According to our model, the present relief on each density contrast has components resulting from loading on all three interfaces

$$H = H_t + H_m + H_b \tag{13a}$$

$$V = V_t + V_m + V_b \tag{13b}$$

$$W = W_t + W_m + W_b, \tag{13c}$$

where H_t is the surface relief due to loading on top of the crust, H_m is the surface relief due to loading on the internal density contrast, V_b is the relief on the internal interface due to loading on the base of the crust, etc. In our model, we have represented loads as relief on the three density contrasts, so the initial loads (or relief before flexure and compensation) are given by

$$H_i = H_t - W_t \tag{14a}$$

$$V_i = V_m - W_m \tag{14b}$$

$$W_i = W_b - H_b. \tag{14c}$$

Separation of the components of relief on the three interfaces is accomplished with the 2-D Fourier transform of the thin plate equation

$$Dk^4U(k) + \rho_m U(k) = Q(k), \tag{15}$$

where Q is the applied load and U is the amplitude of the plate deflection. Using (14) to obtain Q in terms of the components of relief, substitution in (15) yielded expressions for the components of relief. For topographic loading

$$W_t = V_t = -\rho_0 H_t/(\Delta\rho_1 \xi), \tag{16}$$

where ρ_0 is the density of the cover layer and $\Delta\rho_1 = \rho_m - \rho_0$. ξ is a flexural parameter $= 1 + Dk^4/(\Delta\rho_1 g)$. For loading on the internal interface

$$W_m = H_m = -\Delta\rho_2 V_m/[(\rho_m - \Delta\rho_2)\psi], \tag{17}$$

where $\Delta\rho_2 = \rho_c - \rho_0$, ρ_c is the density of the crust. The flexural parameter $\psi = 1 + Dk^4/[(\rho_m - \Delta\rho_2)g]$. For loading by relief on the Moho

$$W_b = -\rho_c H_b \phi/\Delta\rho_3, \tag{18}$$

where $H_b = V_b$, $\Delta\rho_3 = \rho_m - \rho_c$ and $\phi = 1 + Dk^4/(\rho_c g)$.

Substituting (16), (17) and (18) into (13) yields a three by three system for the initial loads H_i, V_i and W_i

$$\Omega = \begin{bmatrix} H_i \\ V_i \\ W_i \end{bmatrix} = \begin{bmatrix} H \\ V \\ W \end{bmatrix}, \tag{19}$$

where the elements of the matrix Ω are given in Table 1. A unique solution of (19) exists if the determinant of Ω does not go to zero. This reduces to a unique solution occuring for $Dk^4 \neq 0$. At wavenumbers where $Dk^4 \simeq 0$, surface and subsurface loads are indistinguishable because all loads are locally compensated and the compensating root cannot be distinguished from the initial load. At these wavenumbers, the topography amplitudes H are assigned to H_c or the locally compensated topography.

Where a solution to (19) does exist, it is possible to predict the coherence between gravity and topography for the assumed value of D. The power of topography is once again given by (2), but with H defined by (13a). Applying (8) to the relief on the two subsurface density contrasts gives the power of gravity

$$E_1 = \langle WW^* \rangle (2\pi\Delta\rho_2 \Gamma)^2 \exp(-2kZ_m) + \langle VV^* \rangle (2\pi\Delta\rho_1 \Gamma)^2 \exp(-2kZ_c), \tag{20}$$

Table 1. Elements of the matrix Ω in (19). See equations (16)–(18) for definitions of symbols

$$\begin{bmatrix} \dfrac{\Delta\rho_1 \xi}{\Delta\rho_1 \xi + \rho_0} & \dfrac{\Delta\rho_3}{\rho_c \phi - \Delta\rho_3} & \dfrac{-\Delta\rho_2}{\Delta\rho_2 + (\rho_m - \Delta\rho_2)\psi} \\ \dfrac{-\rho_0}{\Delta\rho_1 \xi + \rho_0} & \dfrac{\Delta\rho_3}{\rho_c \phi - \Delta\rho_3} & \dfrac{(\rho_m - \Delta\rho_2)\psi}{\Delta\rho_2 + (\rho_m - \Delta\rho_2)\psi} \\ \dfrac{-\rho_0}{\Delta\rho_1 \xi + \rho_0} & \dfrac{-\rho_c \phi}{\rho_c \phi - \Delta\rho_3} & \dfrac{-\Delta\rho_2}{\Delta\rho_2 + (\rho_m - \Delta\rho_2)\psi} \end{bmatrix}$$

where Z_m and Z_c are the depths to the Moho and basement, respectively, and W and V are given by (13b) and (13c). The cross spectrum is

$$C = \langle [W 2\pi\Delta\rho_2 \Gamma \exp(-kZ_m) + V 2\pi\Delta\rho_1 \Gamma \exp(-kZ_c)] H^* \rangle \tag{21}$$

with H, V and W from (13).

Using (5) the predicted coherence reduces to

$$\gamma_p^2 = \frac{\langle H_t W_t \alpha + H_t V_t \beta + H_m W_m \alpha + H_m V_m \beta + H_b W_b \alpha + H_b V_b \beta \rangle^2}{\langle H_t^2 + H_m^2 + H_b^2 \rangle (\langle W_t^2 + W_m^2 + W_b^2 \rangle \alpha^2 + \langle V_t^2 + V_m^2 + V_b^2 \rangle \beta^2)}, \tag{22}$$

where $\alpha = 2\pi\Delta\rho_2 \exp(-kZ_m)$, $\beta = 2\pi\Delta\rho_1 \exp(-kZ_c)$ and the cross terms involving $H_t H_m$ or $H_t V_b$, etc., have been eliminated by assuming that loads on the three interfaces are statistically independent or out of phase. This predicted coherence can then be compared to the observed coherence, and by allowing D to vary it is possible to obtain a least-squares best fit between the two.

Inversion for D

Using the density model of Fig. 8, a least-squares best fit of (22) to the observed coherence was obtained for $D = 1.4 \times 10^{23}$ Nm. This is equivalent to an elastic thickness of $T = 25$ km for a Young's modulus of 10^{11} Nm^{-2}. Fig. 9 shows the coherence predicted by this model compared to the observed coherence. The error bars on the observed coherence are one standard deviation. The observed coherence is within one standard error for over two-thirds of the coherence estimates in the diagnostic waveband where the fall-off occurs, thus the model gives an excellent fit. If acceptable models must simply predict the coherence to within the standard error for at least two thirds of the coherence estimates in the fall-off waveband, the range of possible values for T is 21–30 km. A hypothetical error of 10 km in the depth to the Moho resulted in only a 3 km change in T, and errors in the densities caused very little change in the estimate of T.

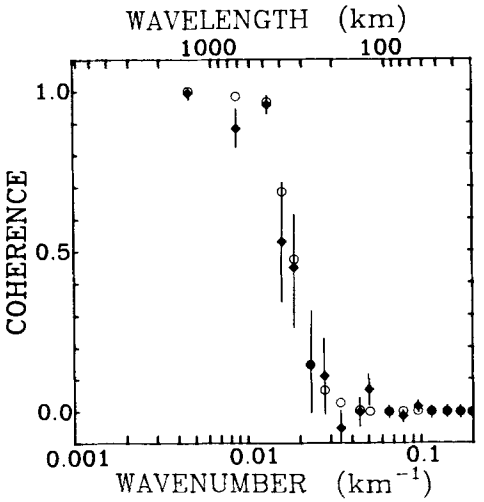

Figure 9. Comparison between the observed coherence (diamonds) and the coherence predicted by the best fitting model (open circles) using the densities and interface depths of Fig. 8 and a flexural rigidity for the lithosphere of 1.4×10^{23} Nm (equivalent effective elastic thickness of 25 km).

The inversion for D was also performed using a simpler model than that of Fig. 8. By downward-continuing all of G to 32 km we considered the case of loading only at the surface and the Moho. The resulting best estimate of T was 30 km with an acceptable range of 25–44 km. Given the uncertainties in the assumptions, this is essentially the same as the result for two subsurface density contrasts. The value of $D = 1.4 \times 10^{23}$ Nm for Kenya is consistent with values of 10^{23}–10^{24} Nm for other continental regions.

Correlation of surface and subsurface loading

Elimination of the cross-terms in (22) is not done just to simplify the equation, but is a consequence of the fundamental assumption of the model that loading on the three interfaces is statistically independent. Only by assuming independence are we able to uniquely determine D. Given any value for D, when we solve for the initial loads on the three interfaces the loads are calculated such that the resulting relief on the interfaces exactly reproduce the observed topography and gravity. Thus, if we were to use the full expression for the predicted coherence rather than (22), we could reproduce the observed coherence exactly for all values of D. However, use of an incorrect D strongly affects the correlation between surface and subsurface loading. Initial loads calculated assuming too high a value of D will reproduce the topography and gravity by having high positive correlation between the surface and subsurface loads. Thus actual flexural features would appear as correlated surface and subsurface loads on a stiff plate. If too low a value of D is assumed, loads with opposite signs for surface and subsurface loading largely cancel each other out to reproduce the gravity and topography. Thus, the correlation between the initial loads will be large and negative. This means that a best-fitting value of D obtained by assuming statistically independent loads and using equation (22) must also minimize the correlation between surface and subsurface loading. Fig. 10 shows the correlation between the amplitudes of surface and subsurface loading for the best fitting value of $T = 25$ km averaged over the same wavebands as the coherence in Figs 4 and 9. As expected, the value

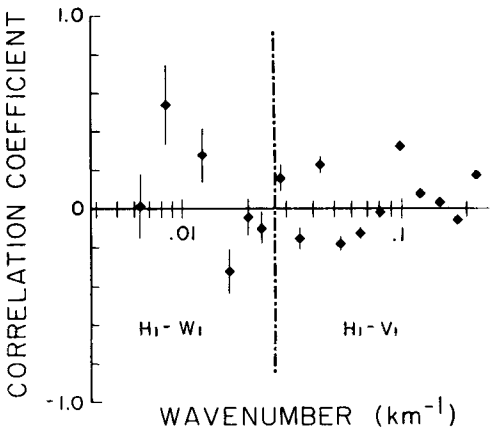

Figure 10. Correlation between the amplitudes of surface and subsurface loads averaged over the same wavebands as the coherence in Figs 4 and 9. Bars represent one standard error for each correlation average. Correlations are generally low, confirming the assumption of overall independence of surface and subsurface loading. Near-zero correlation for the lowest waveband is an artifact due to the inability to distinguish surface and subsurface loading at very long wavelengths.

of T that best fits the coherence is extremely close to the one that minimizes the correlation. Thus we find our best fitting solution using equation (22) to be acceptable.

The residual correlation in Fig. 10 may be due to two things. First, it may represent actual correlation between surface and subsurface loading in Kenya and second, it might indicate that our model of a uniform elastic plate is averaging over some variations in the rigidity of the lithosphere in Kenya. Notice in Fig. 10 that the highest correlations occur for the wavebands where the coherence residuals are largest. These are the wavebands where there may be the most actual correlation between surface and subsurface loading, or the largest effects of a non-uniform T for Kenya. The near zero correlation in the lowest waveband is a result of the Airy-like compensation of long wavelength loads which makes H_i and W_i indistinguishable, and the correlation between the two meaningless.

Intuitively, some correlation between surface and subsurface loading would seem inevitable. For example, magma or partial melting may be responsible for uplifting the Kenya Dome but will also produce volcanism in the same area. The low correlations between surface and subsurface loading that we have observed suggest that a variety of active processes such as doming, volcanic extrusion and intrusion, rifting, erosion and deposition ensure that at most wavelengths, overall surface and subsurface loading are statistically independent when averaged over a large region.

Interpretation of initial loads

The amplitudes of the locally compensated topography H_c, and the initial loads H_i, V_i and W_i were inverse Fourier transformed to obtain the maps of h_c, h_i, v_i and w_i (Figs 11–14). On the load maps, loads have been represented as relief on density contrasts. Thus the contours are in metres, but the surface they represent is not a physical surface. For example,

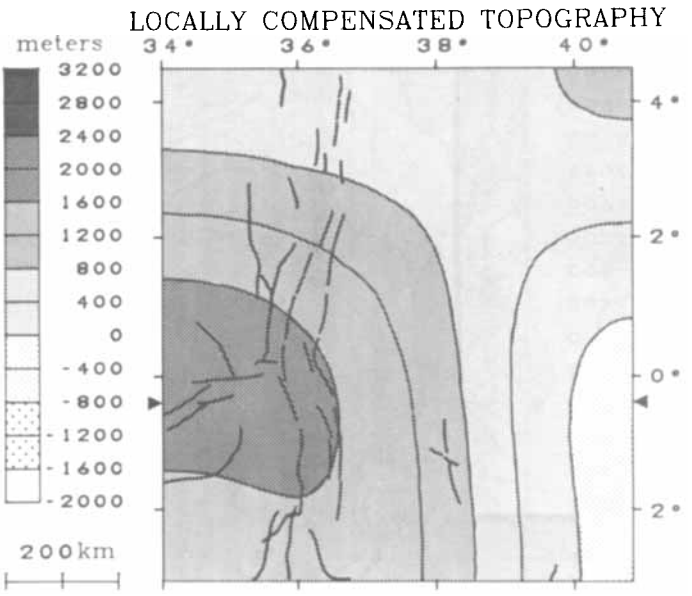

Figure 11. Map of the topography for which surface and subsurface loading are indistinguishable. Represents primarily the westward rise of topography towards the East African Plateau. Arrows mark the end points of the cross-sections of Fig. 15.

w_i represents the load on the lithosphere at depths corresponding to the Moho, but for three reasons this is not a relief map of the Moho itself. First, this is an initial load that will cause deflection resulting in different relief on the Moho. Second, the final relief on the Moho will have components arising from initial loads on the other two interfaces. Finally, the loads that are here represented as relief on a density contrast may actually be the result of lateral density contrasts within the mantle or crust. It is also important to note that since the loads have been represented as the equivalent relief on a density contrast, a given elevation on the surface load map represents a much greater load than the same elevation on either of the subsurface load maps since the density contrast is greatest on the surface.

The map of h_c (Fig. 11) or the locally compensated topography is not a load map. Instead, h_c is the topography that results from loads that are locally compensated. A substantial fraction of the overall relief in Kenya is present in h_c, thus our results support the assumption of Banks & Swain (1978) that East Africa is largely locally compensated. It is impossible to distinguish whether the loads causing the topography at these long wavelengths are surface or subsurface. The locally compensated topography is interpreted as representing primarily the westward rise towards the East African Plateau. Thus the relief of the Kenya Dome will be superimposed on this long-wavelength topography.

The highest amplitude initial surface loads (Fig. 12) are the volcanic cones of Mts Elgon, Kenya and Kilimanjaro. This is a result of the fact that the short-wavelength components of a subsurface load are damped by the rigidity of the plate and cannot create such short-wavelength surface features. Comparison of Fig. 12 with the geological map of Fig. 6 shows a general tendency for the extrusive volcanics of the dome, particularly in the vicinity of Mt Kenya, to appear as surface loads. Thus, these results simply confirm what we already knew from the geology, namely that extrusive volcanics are surface loads on the lithosphere. The fault-bounded rift valley itself also appears largely as a negative surface load. Note in Fig. 12 that the initial loads inside the boundaries of the Gregory Rift are smaller or negative relative

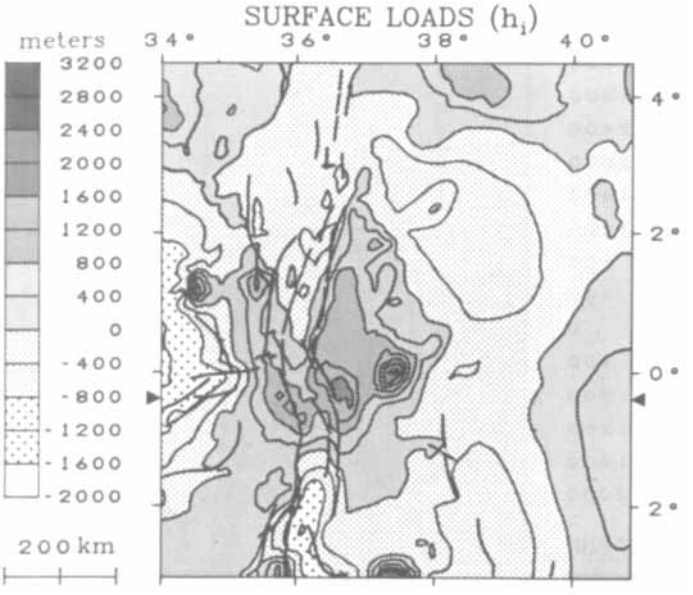

Figure 12. Initial surface load. Note that the volcanic cones of Mts Kenya, Elgon and Kilimanjaro appear as surface loads. Also, comparison with the geology of Fig. 6 shows the extrusive volcanics roughly correlate with surface loads. Arrows mark the end points of the cross sections of Fig. 15.

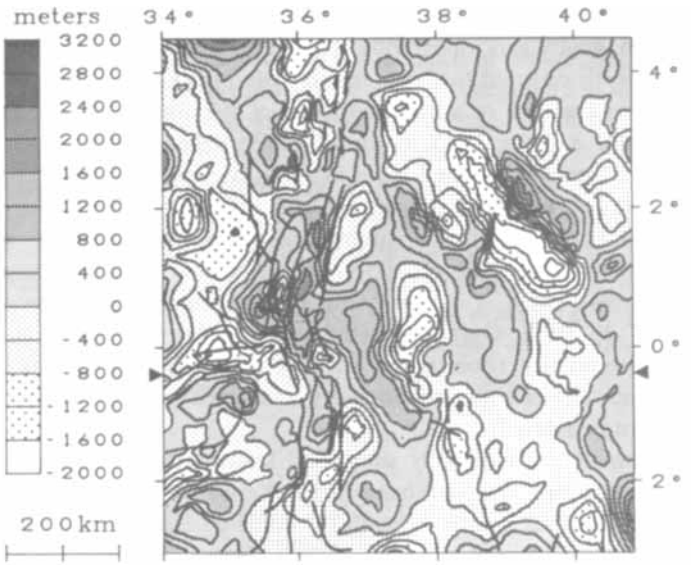

Figure 13. Initial load on the shallow density contrast represented as relief on the interface at 0.5 km depth. Arrows mark the end points of the cross sections of Fig. 15.

to adjacent regions. The short-wavelength topography of such a narrow valley cannot result from subsurface loading and flexure of an elastic plate, thus the process that creates the rift valley appears as surface loading. In reality, since the actual deformation is by faulting rather than flexure, the process that created the rift valley could involve subsurface loading.

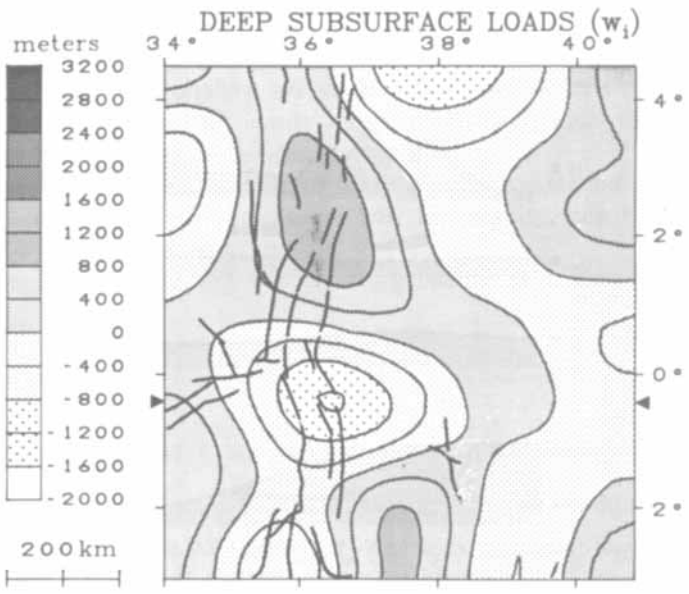

Figure 14. Initial load on the deep density contrast represented as relief on the interface at 32 km depth. Major feature is the upward directed load near the intersection of the Gregory and Kavirondo Rifts that may correspond to a previously identified region of hot, low density mantle. Arrows mark the end points of the cross-sections of Fig. 15.

The map of the regionally supported, shallow, subsurface loading (Fig. 13) is difficult to interpret without further modelling of the effects of various features and processes on the relationship between gravity and topography. There are, however, several features to note. In many places, downward directed loads are found within the Gregory Rift. These may be the loads imposed by the presence of a high density axial dyke in the crust beneath the floor of the rift valley (Savage & Long 1985; Fairhead 1976; Baker & Wohlenberg 1971; Khan & Mansfield 1971). The upward directed loads in the Kavirondo Rift could be due to the low density granites that are visible at the surface and that may underlie the rift (Fairhead & Walker 1979). Mt Kenya, Elgon and Kilimanjaro are all underlain by shallow upward-directed loads or mass deficiences, possibly indicating that elevated temperatures persist beneath the volcanoes. There is currently no explanation for the large positive/negative paired load near 2° W, 39° E. Overlapping the western edge of the load pair is a region of anomalously high seismicity (Pointing *et al.* 1985) and mantle conductivity (Banks & Beamish 1979). Since the seismic, conductivity and gravity anomalies are all unexplained, they may or may not be related.

Fig. 14 is a map of the regionally supported loads at Moho depths. The only major feature is the upwardly directed load beneath the Kenya Dome. The presence of this load indicates that the anomalous mantle beneath the dome does in fact load the lithosphere and cause doming. The highest correlations between surface and subsurface loading occur for wavebands that are seen in Fig. 10 to correspond to wavelengths the size of the Kenya Dome. The correlation is probably the result of the spatial coincidence of doming and extrusive volcanism that has its source in the anomalous mantle.

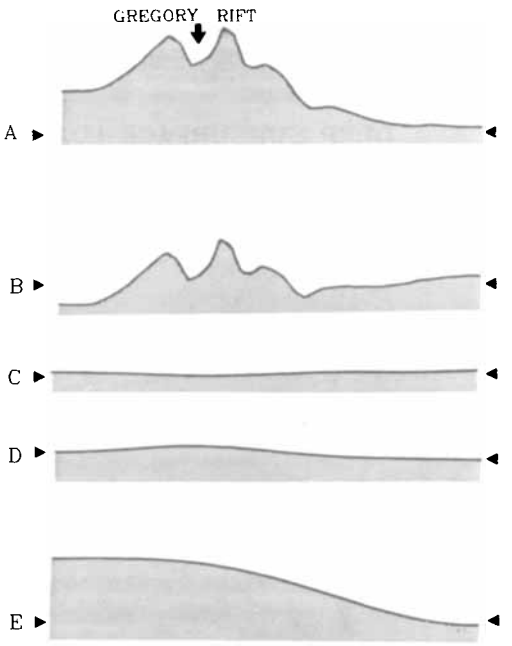

Figure 15. Components of topography along an E–W profile at 0.5° S. (A) topography, (E) component of topography that is locally compensated (represents primarily the westward rise towards the East African Plateau), (B) component of topography due to surface loading and resulting flexure (volcanic construction), (C) component of topography due to shallow subsurface loading and resulting flexure, (D) component of topography due to deep subsurface loading and resulting flexure (doming). The Kenya Dome appears to be largely the result of surface loading.

While the load maps indicate that both surface and subsurface loading contribute to the topography of the Kenya Dome, surface loading is much more important in the development of the dome topography. Fig. 15 depicts the components of topography due to surface and subsurface loading along an E–W profile at 0.5° S. The topography along the profile is the sum of the locally compensated topography h_c, the topography due to surface loading h_t and the topography due to shallow and deep subsurface loading, h_m and h_b. The locally compensated topography reflects mainly the sloped edge of the East African Plateau on which the topography of the Kenya Dome is superimposed. Deep subsurface loading does produce a minor amount of doming, but the main component of the topography of the Kenya Dome is due to surface loading. Although forming a net topographic high, the volcanic load depresses the crust, in agreement with the evidence of downward flexure of the crust beneath the dome from the KRISP profile of Keller *et al.* (1986) and the basement contours of King (1978) and Williams (1978).

Conclusions

(1) The gravity power spectrum suggests that the general density structure beneath Kenya consists of a low-density cover layer averaging 0.5 km thick and an average Moho depth of 32 km. A third density contrast at greater depth may be involved in the local compensation of the very longest wavelength loads on the lithosphere.

(2) The shape of the coherence of gravity and topography versus wavenumber indicates a regional compensation model, in which loads with wavelength greater than about 650 km are locally compensated. For wavelengths between 650 km and 150 km, loads are partially supported by stresses in the lithosphere. Loads with wavelengths less than 150 km are almost completely supported by the strength of the lithosphere.

(3) Inversion of the coherence yields a best fitting effective elastic thickness for the lithosphere in Kenya of 25 km (flexural rigidity of 1.4×10^{23} Nm).

(4) Extrusive volcanics from the rift and volcanic cones, including Mts Kenya, Elgon and Kilimanjaro, act as surface loads on the lithosphere.

(5) Downward directed, shallow subsurface loads within the Gregory Rift may correspond to dykes or other high-density intrusive volcanics, while the upward directed loads in the Kavirondo Rift may be low-density intrusives.

(6) An upward directed, deep subsurface-load near the intersection of the Gregory and Kavirondo Rifts correlates with a region of hot, low density, possibly partially molten mantle detected by other geophysical studies.

(7) The topography of the dome is created primarily by surface loading or volcanic construction.

References

Baker, B. H. & Wohlenberg, J., 1971. Structure and evolution of the Kenya Rift Valley, *Nature,* **229**, 538–542.

Baker, B. H., Mohr, P. A. & Williams, L. A. J., 1972. Geology of the eastern rift system of Africa, *Spec. Pap. geol. Soc. Am.,* **136.**

Banks, R. J. & Beamish, D., 1979. Melting in the crust and upper mantle beneath the Kenya rift: evidence from geomagnetic deep sounding experiments, *J. Geol. Soc. London,* **136**, 225–233.

Banks, R. J. & Ottey, P., 1974. Geomagnetic deep sounding in and around the Kenya rift valley, *Geophys. J. R. astr. Soc.,* **36**, 321–335.

Banks, R. J. & Swain, C. J., 1978. The isostatic compensation of East Africa, *Proc. R. Soc. Lond. A,* **364**, 331–352.

Banks, R. J., Parker, R. L. & Huestis, H. P., 1977. Isostatic compensation on a continental scale: local versus regional mechanisms, *Geophys. J. R. astr. Soc.*, **51**, 431–452.

Baticci, G. & Morgan, P., 1986. New geothermal data from Kenya: implications for seismic structure and velocities, *Eos, Trans. Am. geophys. Un.*, **67**, 1103.

Beamish, D., 1977. The mapping of induced currents around the Kenya rift: a comparison of techniques, *Geophys. J. R. astr. Soc.*, **50**, 311–332.

Bendat, J. S. & Piersol, A. G., 1980. *Engineering Applications of Correlation and Spectral Analysis*, Wiley, New York.

Bonjer, K. P., Fuchs, K. & Wohlenberg, J., 1979. Crustal structure of the East African Rift System from spectral response ratios of long period body waves, *Z. Geophys.*, **36**, 287–297.

Bullard, E. C., 1936. Gravity measurements in East Africa, *Phil. Trans. R. Soc. A*, **235**, 445–531.

Crane, K. & O'Connell, S., 1983. The distribution and implications of heat flow from the Gregory Rift in Kenya, *Tectonophys.*, **94**, 253–276.

Dahlheim, H.-A. & Davis, P. M., 1986. Deep velocity structure beneath the East African Rift and waveform analysis using teleseismic events, *Eos, Trans. Am. geophys. Un.*, **67**, 1103.

Darracott, B. W., Fairhead, J. D. & Girdler, R. W., 1972. Gravity and magnetic surveys in northern Tanzania and southern Kenya, *Tectonophys.*, **15**, 131–141.

Dorman, L. M. & Lewis, B. T. R., 1970. Experimental isostasy. I: Theory of the determination of the Earth's isostatic response to a concentrated load, *J. geophys. Res.*, **75**, 3357–3365.

Fairhead, J. D., 1976. The structure of the lithosphere beneath the eastern rift, East Africa, deduced from gravity studies, *Tectonophys.*, **30**, 269–298.

Fairhead, J. D. & Walker, P., 1979. A detailed gravity study of the crustal structure associated with the Kavirondo Rift Valley, East Africa, in *Geodynamic Evolution of the Afro-Arabian Rift System*, pp. 99–109, ed. Carrelli, A., Italian Geophysical Society.

Forsyth, D. W., 1981. Can the strength of the lithosphere be inferred from the average relationship between topography and gravity anomalies? (abstract), *Eos, Trans. Am. geophys. Un.*, **62**, 1032.

Forsyth, D. W., 1985. Subsurface loading and estimates of the flexural rigidity of continental lithosphere, *J. geophys. Res.*, **90**, 12 623–12 632.

Griffiths, D. H., King, R. F., Khan, M. A. & Blundell, D. J., 1971. Seismic refraction line in the Gregory Rift, *Nature*, **229**, 66–71.

Halderman, T. P., Davis, P. M. & Dahlheim, H.-A., 1986. *Q* estimates of the asthenospheric upwarp beneath the Rio Grande and the East African Rifts, *Eos, Trans. Am. geophys. Un.*, **67**, 1103.

Haxby, W. F., Turcotte, D. L. & Bird, J. M., 1976. Thermal and mechanical evolution of the Michigan Basin, *Tectonophys.*, **36**, 57–75.

Isaac, G. L., 1967. Stratigraphy of the Peninj group – early middle Pleistocene formations west of Lake Natron, Tanzania, in *Background to Evolution in Africa*, pp. 229–258, eds Bishop, W. W. & Clark, J. D., Chicago University Press.

Karner, G. D. & Watts, A. B., 1983. Gravity anomalies and flexure of the lithosphere at mountain ranges, *J. geophys. Res.*, **88**, 10 449–10 477.

Keller, G. R., Khan, M. A. & Prodehl, C., 1986. Crustal structure in the Kenyan portion of the East African Rift, *Eos, Trans. Am. geophys. Un.*, **67**, 1103.

Khan, M. A. & Mansfield, J., 1971. Gravity measurements in the Gregory Rift, *Nature*, **229**, 72–75.

King, B. C., 1978. Structural and volcanic evolution of the Gregory Rift Valley, in *Geological Background to Fossil Man*, ed. Bishop, W. W., Scottish Academic Press, Edinburgh.

Knopoff, L. & Schlue, J. W., 1972. Rayleigh wave phase velocities for the path Addis Ababa to Nairobi, *Tectonophys.*, **15**, 157–163.

Long, R. E. & Backhouse, R. W., 1976. The structure of the western flank of the Gregory Rift. II. The mantle, *Geophys. J. R. astr. Soc.*, **44**, 677–688.

Louden, K. E. & Forsyth, D. W., 1982. Crustal structure and isostatic compensation near the Kane fracture zone from topography and gravity measurements: Part I: Spectral analysis approach, *Geophys. J. R. astr. Soc.*, **68**, 725–750.

Maguire, P. K. H. & Long, R. E., 1976. Structure on the western flank of the Gregory Rift. I. The crust, *Geophys. J. R. astr. Soc.*, **44**, 661–675.

McCall, G. J. H., Baker, B. H. & Walsh, J., 1967. Late Tertiary and Quarternary sediments of the Kenya rift valley, in *Background to Evolution in Africa*, pp. 191–220, eds Bishop, W. W. & Clark, J. D., Chicago University Press.

McKenzie, D. P. & Bowin, C., 1976. The relationship between bathymetry and gravity in the Atlantic ocean, *J. geophys. Res.*, **81**, 1903–1915.

McNutt, M. K., 1980. Implications of regional gravity for state of stress in the Earth's crust and upper mantle, *J. geophys. Res.*, **85**, 6377–6396.

McNutt, M. K., 1983. Influence of plate subduction on isostatic compensation in Northern California, *Tectonics*, **2**, 399–415.

McNutt, M. K. & Parker, R. L., 1978. Isostasy in Australia and the evolution of the compensation mechanism, *Science*, **199**, 773–775.

Munk, W. H. & Cartwright, D. E., 1966. Tidal spectroscopy and prediction, *Phil. Trans. R. Soc. A*, **259**, 533–589.

Nakiboglu, S. M. & Lambeck, K., 1983. A reevaluation of the isostatic rebound of Lake Bonneville, *J. geophys. Res.*, **88**, 10439–10447.

Nolet, G. & Mueller, St., 1982. A model for the deep structure of the East African rift system from simultaneous inversion of teleseismic data, *Tectonophys.*, **84**, 151–178.

Passey, Q. R., 1981. Upper mantle viscosity derived from differences in rebound of the Provo and Bonneville shorelines: Lake Bonneville Basin, Utah, *J. geophys. Res.*, **86**, 11 701–11 708.

Pointing, A. J., Maguire, P. K. H., Khan, M. A., Francis, D. J., Swain, C. J., Shar, E. R. & Griffiths, D. H., 1985. Seismicity of the northern part of the Kenya Rift Valley, *J. Geodyn.*, **3**, 23–38.

Ringwood, A. E., 1975. *Composition and Petrology of the Earth's Mantle*, McGraw-Hill, New York.

Rooney, D. & Hutton, V. R. S., 1977. A magnetotelluric and magnetovariational study of the Gregory Rift Valley, Kenya, *Geophys. J. R. astr. Soc.*, **51**, 91–119.

Rykounov, L. N., Sedov, V. V., Savrina, L. A. & Bourmin, V. Ju., 1972. Study of micro-earthquakes in the rift zones of East Africa, *Tectonophys.*, **15**, 123–130.

Saggerson, E. P. & Baker, B. H., 1965. Post-Jurassic erosion surfaces in eastern Kenya and their deformation in relation to rift structure, *Q. Jl geol. Soc. Lond.*, **121**, 51–72.

Savage, J. E. G. & Long, R. E., 1985. Lithospheric structure beneath the Kenya Dome, *Geophys. J. R. astr. Soc.*, **82**, 461–477.

Sayles, R. S. & Thomas, T. R., 1978. Surface topography as a nonstationary random process, *Nature*, **271**, 431–434.

Searle, R. C., 1970. Evidence from gravity anomalies for thinning of the lithosphere beneath the rift valley in Kenya, *Geophys. J. R. astr. Soc.*, **21**, 13–31.

Skinner, N. J., 1977. Recent geophysical studies of the Kenya Rift Valley, *Contemp. Phys.*, **18**, 455–470.

Swain, C. J., 1979. Gravity and seismic measurements in Kenya, *PhD thesis*, University of Leicester.

Swain, C. J. & Khan, M. A., 1978. Gravity measurements in Kenya, *Geophys. J. R. astr. Soc.*, **53**, 427–429.

Swain, C. J., Khan, M. A., Wilton, T. J., Maguire, P. K. H. & Griffiths, D. H., 1981. Seismic and gravity surveys in the Lake Baringo–Tugen Hills area, Kenya Rift Valley, *J. Geol. Soc. London*, **138**, 93–102.

Walcott, R. I., 1970. Flexural rigidity, thickness and viscosity of the lithosphere, *J. geophys. Res.*, **75**, 3941–3954.

Williams, L. A. J., 1978. The volcanological development of the Kenya Rift, in *Petrology and Geochemistry of Continental Rifts*, pp. 101–121, eds Neumann, E.-R. & Ramberg, I. B., Reidel, New York.

Woollard, G. P., 1970. Evaluation of the isostatic mechanism and role of mineralogic transformations from seismic and gravity data, *Phys. Earth planet. Int.*, **3**, 484–498.